BL-16A/2018P011

Magnetic reversal in $Mn_{4-x}Ni_xN$ films measured via X-ray magnetic dichroism

Taro KOMORI[1], Kenta AMEMIYA[2], and Takashi SUEMASU[1,*]
[1] University of Tsukuba, 1-1-1 Tennohdai, Tsukuba, Ibaraki, 305-8573, Japan
[2] Photon Factory, Institute of Materials Structure Science,
High Energy Research Organization,
1-1 Oho, Tsukuba, 305-0801, Japan

1 Introduction

Ferrimagnets have attracted increasing attention for their applications to spintronics devices. There are some ferrimagnets possessing a magnetic (angular momentum) compensation point since their key feature is that the magnetic moments of their sublattices are aligned antiparallel to each other. Spin transfer torque (STT) and spin orbit torque (SOT) are composed of a flux of angular momentum carried by an incoming spin current and absorbed by the magnetization. In ferrimagnets close to the angular momentum compensation point, the switching is eased and the critical current densities decrease, and thus this can be applied to current-induced domain wall motion (CIDWM) assisted by STTs and SOTs. Thus far, there have been many studies on ferrimagnets consisting of both transition-metal and rare-earth (RE) elements. For instance, a domain wall velocity of 1.3km/s assisted by both STTs and SOTs has been achieved in $Gd_{44}Co_{56}$ at 260 K [1]. However, there have been no reports of ferrimagnets without RE elements possessing a compensation temperature close to room temperature (RT). Under such circumstances, we have focused on RE-free ferrimagnet Mn_4N films [2-4].

Figure 1 shows the crystal structure of Mn_4N. The corner and face-centered atomic sites are labelled as I and II, respectively. The II sites are further divided into IIA and IIB sites in the presence of magnetization (arrow in Fig. 1). N atoms are at the body-centered sites. Neutron diffraction measurement shows the magnetic moments of the Mn atoms in bulk Mn_4N to be 3.53 μ_B at I sites and −0.89 μ_B at II sites with the easy magnetization axis along the [111] direction [5,6], where μ_B is the Bohr magneton. Mn_4N films have perpendicular magnetic anisotropy (PMA) with relatively a large magnetic anisotropy constant of approximately 10^5 J/m^3. We have recently achieved a velocity of approximately 900 m/s with a current density of 1.2×10^{12} A/m^2 at RT [7], which is a record velocity for CIDWM only by STT. Thus, mixed crystal nitride films based on Mn_4N are expected to have both PMA with low saturation magnetization (M_S) and a compensation point, leading to more efficient domain wall motion. Compared with Mn_4N, $Mn_{4-x}Ni_xN$ films have shown an anomalous decrease in M_S of 45% at x = 0.1 and 75% at x = 0.25, while the PMA is preserved. It is noted that the tensile stress is present in the $Mn_{4-x}Ni_xN$ films with PMA. We further concluded that $Mn_{4-x}Ni_xN$ films have a magnetic compensation composition at RT because the signs of the anomalous Hall resistivity and M_S temperature dependences were different between x = 0.1 and 0.25 [8]. The latter two trends were also similar to those of $Mn_{4-x}In_xN$ and $Mn_{4-x}Sn_xN$, in which Mekata demonstrated the existence of a magnetic compensation point [9]. However, the magnetic structures and preferential occupation sites of Ni atoms in $Mn_{4-x}Ni_xN$ epitaxial films are not yet known. X-ray absorption spectroscopy (XAS) and X-ray magnetic circular dichroism (XMCD) are powerful techniques for determining element-specific electronic structures.

In this work, we performed XAS and XMCD measurements on $Mn_{4-x}Ni_xN$ (x = 0.1, 0.25) epitaxial films, and proposed a model describing the magnetic moments of Ni and Mn atoms below and above the Ni magnetic compensation composition in $Mn_{4-x}Ni_xN$ films.

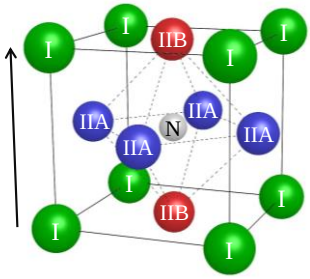

Fig. 1: Crystal structure of Mn_4N. Face-centered sites (II) can be further divided into IIA and IIB sites with magnetization (arrow).

2 Experiment

We grew approximately 10-nm-thick $Mn_{4-x}Ni_xN$ (x = 0.1 and 0.25) epitaxial films on $SrTiO_3$[STO](001) substrates by molecular beam epitaxy, using high-temperature Knudsen cells with solid Mn and Ni sources and a radio-frequency N plasma source [4]. After growth, the samples were capped in situ with Ti to prevent oxidation. XAS and XMCD measurements were performed at the twin APPLE-II undulator beam line BL-16A of KEK in Japan. Both a magnetic field of ±3 T and circularly polarized x rays with left or right polarization were applied perpendicularly to the plane. The x-ray polarization was switched at every energy point with a frequency of 10 Hz using five kicker magnets. Spectra were acquired at RT in total electron yield mode and total fluorescence yield mode at the Mn $L_{2,3}$ and Ni $L_{2,3}$ absorption edges, respectively, in order to prevent Ni $L_{2,3}$ spectra from overlapping with background signals.

3 Results and Discussion

Figures 2(a)(e) and 2(b)(f) show the XAS and XMCD spectra of $Mn_{3.9}Ni_{0.1}N$ and $Mn_{3.75}Ni_{0.25}N$ films at the Ni $L_{2,3}$ and Mn $L_{2,3}$ absorption edges, respectively. Figures 2(c) and 2(d) are those for Ni_3FeN and $NiFe_3N$ films at the Ni $L_{2,3}$ absorption edges, respectively. Concerning the XAS spectra of $Mn_{3.9}Ni_{0.1}N$ and $Mn_{3.75}Ni_{0.25}N$ films in Figs. 2(a) and 2(b), only the sharp main peaks appear at the L_3 edge (852–853 eV) and the L_2 edge (870 eV). In contrast, we see shoulders in the XAS spectrum of Ni-rich Ni_3FeN films in Fig. 2(c) [10].

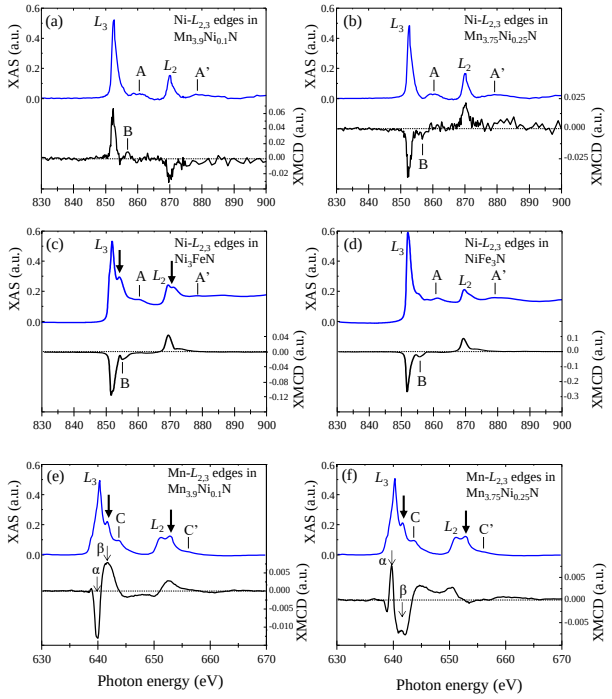

Fig. 2: XAS (blue) and XMCD (black) spectra in (a)(e) $Mn_{3.9}Ni_{0.1}N$ films and (b)(f) $Mn_{3.75}Ni_{0.25}N$ films at Ni-$L_{2,3}$ and Mn-$L_{2,3}$ absorption edges, respectively. (c) and (d) are those for Ni3FeN and NiFe3N films at Ni-$L_{2,3}$ absorption edges.

Such shoulders are observed approximately 2 eV above the Ni $L_{2,3}$ main peaks, and are reported for other antiperovskite ferromagnetic nitrides such as Fe_4N and Co_4N films above the Fe (Co) $L_{2,3}$ main peaks [11,12]. These are interpreted to originate from the electric dipole transition from the metal 2*p* core level to the hybrid state between the orbitals of the N 2*p* and metal 3*d* at II sites. These results indicate that the objective element is at II sites [11]. However, we don't see these shoulders in the XAS spectrum of $NiFe_3N$ films in Fig. 2(d). It is reported that in $Ni_xFe_{4-x}N$, the preferential sites of Ni atoms determined by XAS measurements agree well with those obtained via Mössbauer measurements and first-principles calculations based on the configuration-dependent total energy [10]. Thus, we have a reasonable confidence in the results obtained for $Mn_{4-x}Ni_xN$ as well. From these results, it can be safely stated that Ni atoms preferentially occupy the I sites in Mn_4N when $x \leq 0.25$. In addition to the shoulders mentioned above, Figs. 4(a)–4(d) show other distinct satellites marked as A and A'. Satellites A and A' are observed at approximately 7 eV above the Ni L_3 and L_2 edges. We initially considered their origin to be the hybrid state between the Ni 3*d* and O 2*p* orbitals. However, these are rather close to the satellite positions reported for the Ni $L_{2,3}$ edges of $Ni_xFe_{4-x}N$.

In contrast to XAS spectra, the XMCD spectra for Ni are simple. The peak signs are opposite at the $L_{2,3}$ edges between $Mn_{3.9}Ni_{0.1}N$ and $Mn_{3.75}Ni_{0.25}N$ in Figs. 2(a) and 2(b). Thus, the directions of magnetic moments of Ni(I) in $Mn_{3.9}Ni_{0.1}N$ films are different with that in $Mn_{3.75}Ni_{0.25}N$ films with respect to magnetizations. Regarding satellites B in Figs. 4(a)-4(d), it has been found only experimentally. This can be understood by considering that satellite B results from the interaction between the final-state multiples described with $2p^53d^9$ and $2p^53d^{10}$. Although no distinct satellite is observed in the XMCD spectra above the Ni L_2 edges, it has been experimentally confirmed elsewhere [13]. We conclude that the satellite intensity is weak owing to the small atomic ratio of Ni, and that the satellites are buried in background signals.

We next move on to the XAS and XMCD spectra of $Mn_{3.9}Ni_{0.1}N$ (Fig. 4(e)) and $Mn_{3.75}Ni_{0.25}N$ films (Fig. 4(f)) at the Mn $L_{2,3}$ absorption edges. Shoulders marked by arrows and satellites (C,C') are observed at approximately 2 eV and 3.5 eV, respectively, above the Mn $L_{2,3}$ main peaks of the $Mn_{3.9}Ni_{0.1}N$ and $Mn_{3.75}Ni_{0.25}N$ films. Note that similar features were observed in the XAS spectra of Mn-related oxides such as $MnFe_2O_4$ [14], and are characterized by the final state multiples of the $2p^53d^6$ configuration from a highly localized Mn^{2+} ground state.

The XMCD spectra of these films also show some complexity. The signs of the XMCD signals around the Mn L_3 edge are positive, negative, and positive from low to high photon energy in $Mn_{3.9}Ni_{0.1}N$. The superposition of spectra with different signs indicates that the magnetic moments of Mn(I) and Mn(II) are aligned antiparallel to each other. In our previous studies on Fe_4N films, the transition metals at the I(II) site exhibit localized (itinerant) states supported by the first-principles calculation using the all-electron full-potential linearized augmented-plane-wave (FLAPW) method and Fermi's golden rule with E1 transitions [15]. Similar calculation results are also supported for Mn_4N by the FLAPW calculation [16]. Therefore, the XMCD spectra of $Mn_{3.9}Ni_{0.1}N$ and $Mn_{3.75}Ni_{0.25}N$ films can also be viewed as an overlap of such localized and itinerant components characterized by features α and β, respectively, with opposite signs. In

$Mn_{3.9}Ni_{0.1}N$, the broad positive peak (β) near 642 eV likely originates from Mn(II) atoms because of the hybridization between Mn(II) 3*d* and N 2*p* orbitals. In contrast, the sharp negative peak (α) near 640 eV likely comes from Mn(I), which is remote from N, and therefore entails less hybridization. Note that the signs of the XMCD signals near the Mn L_3 absorption edges are negative, positive, and negative from low to high photon energy in $Mn_{3.75}Ni_{0.25}N$, which is the opposite of the results obtained for the $Mn_{3.9}Ni_{0.1}N$ films. We ascribe this to magnetization reversal at both I and II sites. It is also notable that the XMCD signal at the Ni L_3 absorption edge has the opposite sign of the sharp peak for the Mn L_3 edge at 640 eV regardless of *x*, and has the same sign as that of the broad spectrum at 642 eV. The former mainly comes from Mn(I) atoms and the latter from Mn(II) atoms. Thus, the magnetic moments of Ni(I) always align in parallel with those of Mn(II) or in antiparallel with those of Mn(I) in the studied range of *x*.

On the basis of these discussions, we conclude that the preferential occupation site of Ni is the I site in $Mn_{4-x}Ni_xN$ thin films, and that the magnetic moments of Ni atoms are parallel to those of Mn(II). As mentioned in Fig. 1, Mn_4N is a ferrimagnetic material in which the magnetic moments of the Mn(I) atoms are aligned parallel to the magnetic field *H* and antiparallel to the moments of the Mn(II) atoms. The magnetic moments of the Mn(I) sites thus determine the direction of M_S. For $x = 0.1$, some Mn(I) atoms are replaced with Ni atoms, and the magnetic moments of the Ni(I) atoms are parallel to those of Mn(II). This results in a net decrease in M_S [8], and the Mn(I) atoms still determine the direction of M_S. When *x* is increased further to 0.25, more Mn(I) atoms are replaced with Ni atoms to the extent where the sum of the magnetic moments aligned antiparallel to magnetic field becomes greater than that of those aligned parallel to it. In this state, the net magnetization and magnetic field are antiparallel, causing an unstable Zeeman energy state. Thus, all magnetic moments need to flip to achieve the stable state. As a result, the magnetic moments of the Mn(II) sites determine the direction of M_S at $x = 0.25$. Therefore, we can safely state that the magnetic compensation occurs at a value of *x* between 0.1 and 0.25.

Acknowledgement

This work was supported by Grants-in-Aid for Scientific Research from the Japan Society for the Promotion of Science (Nos. 19K04499, 19K21954, and 19KK0104). The XMCD experiment was performed at beam line BL-16A of KEK-PF with the approval of the Photon Factory Program Advisory Committee (Proposal No. 2018P011).

References

[1] L. Caretta *et al*., *Nat. Nanotechnol.* **13**, 1154 (2018).
[2] Y. Yasutomi *et al*., *J. Appl. Phys*. **115**, 17A935 (2014).
[3] K. Ito *et al*., *AIP Adv*. **6**, 056201 (2016).
[4] T. Komori *et al*., *J. Cryst. Growth* **507**, 163 (2019).
[5] W. J. Takei *et al*., *Phy. Rev. B* **125**, 1893 (1962).
[6] C. Li *et al*., *J. Alloys. Compd*. **457**, 57 (2008).
[7] T. Gushi *et al*., *Nano Lett.* **19**, 8716 (2019).
[8] T. Komori *et al*., *J. Appl. Phys.* **125**, 213902 (2019).
[9] M. Mekata, *J. Phys. Soc. Jpn*. **17**, 5 (1962).
[10] F. Takata *et al*., *Phys. Rev. Mater.* **2**, 024407 (2018).
[11] K. Ito *et al*., *J. Appl. Phys*. **117**, 193906 (2015).
[12] K. Ito *et al*., *J. Appl. Phys*. **115**, 11C712 (2014).
[13] T. Jo and G. A. Sawatzky, *Phys. Rev. B* **43**, 8771 (1991).
[14] J.-S. Kang *et al*., *Phys. Rev.* B **77**, 035121 (2008).
[15] K. Ito *et al*., *J. Appl. Phys*. **117**, 193906 (2015).
[16] K. Ito *et al*., *Phys. Rev. B* **101**, 104401 (2020).

* suemasu@bk.tsukuba.ac.jp